Conjugate Faulting, Stepover, and Inflation Associated with the 2010 Magnitude 7.2 El Mayor-Cucapah Earthquake Observed in UAVSAR and GPS Measurements

Andrea Donnellan

Jet Propulsion Laboratory, California Institute of Technology and

University of Southern California

Jay Parker, Scott Hensley, Bruce Bills, Brian Hawkins, Paul Rosen, Yang Zheng, Yunling Lou

Jet Propulsion Laboratory, California Institute of Technology

John Rundle

University of California Davis

Tom Herring

Massachusetts Institute of Technology

Lisa Grant Ludwig

University of California, Irvine

Marlon Pierce, Geoffrey Fox, Yu Ma, Jun Wang

Indiana University

Dennis McLeod, Rami Al-Ghanmi

University of Southern California

Alessandro Grippo

Santa Monica College

Submitted to Geochemisty, Geophysics, Geosystems, October 10, 2011

Abstract

GPS and UAVSAR observations of the April 2010 M 7.2 El Mayor – Cucupah earthquake indicate a pattern of substantial deformation and sympathetic fault slip associated with the rupture. A series of conjugate left-lateral faults slipped in association with the earthquake and continued to slip into December 2010. A right-lateral stepover developed to the northwest of the main-shock rupture connecting the Laguna Salada and Elsinore faults. Slip on this stepover occurred at a depth of 2-10 km and also continued postseismically. Further northeast the Superstition Hills fault slipped 2 cm at the surface and the Imperial Fault slipped 4 cm. Both slipped right-laterally. The pairs of data that make up the UAVSAR interferogram were collected in October 2009 and April 2011, so it is not possible to determine whether these right-lateral slip events occurred during the coseismic event. The UAVSAR data show an elliptical fringe pattern across the Imperial Valley that is generally matched by a broad pattern of uplift observed in the GPS data, perhaps indicating a regional intrusion of water or magma. About 20 mm of uplift occurred in the Salton Trough surrounding the main shock and an additional 7 mm of uplift occurred in the April – July 2010 timeframe in the southern part of the Imperial Valley. The GPS station closest to the rupture subsided during the earthquake, but began uplifting in March 2011. The uplift pattern and conjugate sets of faults are reflective of the transition zone from rifting in the Gulf of California to transform plate boundary motion between the Pacific and North American plates.

Introduction

The 4 April 2010, M 7.2 El Mayor-Cucapah earthquake occurred in northern Baja, Mexico on a northwest-southeast trending right-lateral oblique normal fault [Hauksson et al, 2010]. The fault ruptured the surface and extended just south of the border between Baja and California. The region was observed by continuous GPS (Global Positioning System), and with UAVSAR (Uninhabited Autonomous Vehicle Synthetic Aperture Radar) beginning in October of 2009 and several times following the earthquake, providing detailed coseismic and postseismic images of surface deformation.

About 42 mm/yr of shear deformation occur across southern California between Palm Springs and the Mexican border [Meade and Hager, 2005, Fay and Humphreys, 2005]. In this region the San Andreas fault is slipping at about 25 mm/yr, the San Jacinto Fault at 12 mm/yr, and the Elsinore fault at about 4 mm/yr [Weldon and Sieh, 1985; Blisniuk et al., 2010; Rockwell et al., 1990; Millman and Rockwell, 1986; WGCEP, 2008; Fay and Humphreys, 2005]. This area, to the north of the Gulf of California, is a transition zone between the extensional tectonic regime of the East Pacific Rise and the transform tectonics of the strike-slip San Andreas fault system (Figure 1A). Both tectonic regimes (extension and transform) are manifest in the Imperial Valley and Salton Trough by abundant seismicity along northwest-trending right-lateral strike-slip faults and northeast-trending left-lateral conjugate faults, with swarms of shallow earthquakes in the Brawley seismic zone southeast of the Salton Sea [Nicholson et al., 1986, Irwin, 1990]. The Salton Trough is characterized by high heat flow, Quaternary volcanism, and hydrothermal activity associated with magma intrusion at shallow depth [Irwin, 1990; Hill et al., 1990].

The paleoseismic and historic records show the region is capable of producing large earthquakes, such as the southern San Andreas fault rupture in ~1700 A.D. [WGCEP, 2008], and sequences of earthquakes. The 1940 M_w7.0 El Centro and 1979 M_w6.5 Imperial Valley earthquakes ruptured overlapping sections of the Imperial fault [Toppozada et al., 2002] and the 1968 M_w6.6 Borrego Mountain earthquake triggered slip on the Superstition Hills fault [Nicholson et al., 1986]. The northwest-trending Superstition Hills fault, a branch of the San Jacinto fault zone, subsequently ruptured in 1987 in a M_w 6.6 earthquake which was preceded a few hours by the M_w 6.2 Elmore Ranch earthquake on the conjugate northeast-trending Elmore Ranch fault [Hudnut et al., 1989; Hill et al., 1990]. The southern Elsinore fault zone has not ruptured historically. The southern Coyote Mountains segment of the Elsinore fault zone is separated from the northern Laguna Salada fault zone, which ruptured in 1892, by a releasing stepover with several northeast-trending cross-faults [WGCEP, 2008].

The actively deforming Salton Trough, which includes northern Baja, the Salton Trough, and areas west of the Salton Trough, was identified as a location of increased earthquake probabilities or hotspots [Holliday et al, 2007] based on methods derived from pattern informatics forecasting methodology developed by Rundle and Tiampo [Rundle et al, 2002; Tiampo et al, 2002; Rundle et al, 2003]. The effectiveness of the Pattern Informatics method was tested in a prospective test from January 1, 2006 - December 31, 2010. It was found to have considerable skill at locating the future earthquakes M>4.95 that occurred during the test period [Lee et al, 2011].

A UAVSAR experiment to observe the Imperial Valley transition zone between the Gulf of California and the San Andreas fault system (Figure 1A) was initiated because of the predicted increase in earthquake probability combined with large earthquakes in the past and active deformation on several faults in the region. Because the deformation is primarily on northwest-southeast striking right-lateral faults, we designed the UAVSAR experiment with flight swaths perpendicular to the faults in order to observe maximal range changes associated with displacements along the faults. As a result observations were collected over the region prior to the El Mayor – Cucupah earthquake, and several times following the event.

UAVSAR and GPS Observation of the El Mayor/Cucapah Earthquake

The NASA/JPL UAVSAR is an airborne, L-band, fully polarimetric radar housed in a pod that is mounted to the belly of a Gulfstream III aircraft. UAVSAR employs a precision autopilot that allows the plane to fly a specified flight path within a 5 m tube, and an electronically scanned antenna with beam steering based on inertial navigation unit (INU) data. These capabilities facilitate repeat pass interferometric radar observations. The instrument observes approximately 22 km wide swaths that are typically between 100 km and 300 km long. Interferometric radar images (or interferograms) are generated from repeat passes flown over a desired site. UAVSAR requires additional processing compared to spaceborne data because the aircraft trajectories are often compromised by wind gusts and turbulence. Motion compensation guided by integrated GPS/INU measurements of 2-3 cm position accuracy is an order of magnitude less accurate than what is needed for geodetically useful observations. To overcome this difficulty, offset measurements between single look complex (SLC) images from the two passes are used to solve for the residual baseline, velocity and attitude angles. Motion data are corrected and the imagery reprocessed [Hensley et al, 2008]. Products generated by the UAVSAR processor include both slant range multilooked interferograms and unwrapped phase products, with 36 looks and approximately 6-7 m postings, as well as the corresponding geocoded data products in geographic coordinates based on the SRTM 30 m DEM.

UAVSAR data were first collected for the Salton Trough experiment along the border on 20 October 2009 (Table 1). The El Mayor-Cucapah earthquake ruptured northward in Baja, Mexico to the border between the US and Mexico, while the UAVSAR observations were collected in the US to the border of Mexico. As a result, UAVSAR observes only the northern terminus of the rupture, and associated crustal deformation response to the north. Repeat pass data were collected on 12 and 13 April 2010 about one week after the M 7.2 El Mayor-Cucapah earthquake, on 1 July 2010 and 1 December 2010 (Figure 1), making it possible to construct repeat pass interferometric (RPI) products for the mainshock, and near term postseismic deformation.

Data were also collected in April 2009, and September 2010, but are not used in this study. In the first case, the observations were further north across the Imperial Valley and are too far north to show co- or postseismic motions. For the latter case, the RPI product is noisy suggesting too many error sources to make a useful product.

GPS data are also continuously collected for this region and were used in part to constrain some characteristics of the phase unwrapped repeat pass interferometry products, and also highlight a pattern of uplift in the Imperial Valley. Up to 2 cm of uplift occurred spanning the earthquake. Motion continued, at a lower level, at least to the July 1, 2010 time period in the southern part of the Salton Trough, and uplift started in Spring of 2011 near the mainshock rupture and Mexican border.

The southernmost interferogram (Line 26501) shows two lobes of deformation, marking the north end of the rupture near the Mexican border. The data were examined in a variety of ways to understand the robustness of the solution. The east lobe and localized discontinuities, or offsets, are reflective of ground motion. However error sources from atmospheric water vapor or aircraft motion estimation may be obscuring the deformation in the western part of the interferogram.

The earthquake caused large offsets of the ground in the region of this line, which could contaminate the aircraft residual motion estimates. 2D pixel offsets between the two images via amplitude correlation of tiles is computed. A model relates the image offsets to a residual baseline slope. The slope is integrated in time to give the relative motion error. The error is assumed to have zero mean and as a result half of the error is added to each flown track. The data are then reprocessed with the updated motion for the final products. When the deformation signal is large compared to a pixel, there is a possibility of corrupting the offset measurement and thus the estimated motion. The ~ 8 cm amplitude western lobe has widely different characteristics for different solutions, while the ~80 cm amplitude eastern lobe and other features persist for various solutions.

A bound on the error due to atmospheric water vapor may be estimated by examining records of wet troposphere delay [Moore et al, 2010] estimated during the days of flight at local GPS stations. We take the temporal variations of these estimates as proxies for the spatial variability of the water vapor signal in the UAVSAR displacement maps. Differencing the records for the flight dates at stations and taking the extreme values at P494 and P500 (at the western and eastern boundary of the agricultural land, respectively), we estimate the upper bound for vertical water vapor 2-way delay error to be 9.0 cm at P474 and 5.4 cm at P500. This vertical error bound scales according to the increased ray path for off-vertical illumination of pixels, proportional to the cosecant of the elevation angle. This approximately doubles these error bounds in the part of the image farthest from the flight path. Actual errors in radar deformation are likely to be substantially smaller than these bounds, as we have not removed diurnal variation (temporal variation is likely larger than spatial variation during a data capture).

Left-lateral offsets of the fringes can be seen, including along a well-defined discontinuity, which is conjugate to the mainshock rupture and corresponds to the location of the Yuha Fault. The Yuha fault [Treiman, 2011] is one of a series of northeast-trending cross-faults [Nicholson et al., 1986] between major strands of the southern Elsinore and Laguna Salada fault zones. In addition to the Yuha fault, a number of northwest and northeast striking offsets that are conjugate to each other can be noted in the interferogram (Figures 2A and 7A). The eastern lobe shows more data outages due to temporal decorrelation in the Imperial Valley from active cultivation of agricultural fields. This lobe of deformation shows disturbance on its eastern margin, which may be due to leveling or settling of the Imperial Valley from liquefaction. Soil moisture effects, which are not unlikely given the extensive liquefaction of the area [McCrink et al, 2011] can also be a contributing source of error to the results. Northwest striking linear offsets in the interferogram can be observed on both the Imperial fault (line 26501 ellipsoid in Figure 1B) and on the Superstition Hills fault (line 26505 in figure 2A).

East of the two lobes a large elliptical fringe pattern tens of kilometers across can be seen in both line 26501 and the next line north (26505). The elliptical pattern (Figure 1A) could be attributed to atmosphere, residual, aircraft motion, or crustal motion. Uplift of 1–2 cm is observed at the GPS stations for the same time period as that spanned by the coseismic interferogram (20/10 October 2009 – 12/13 April 2010), and about 7 mm of uplift is observed in the GPS stations for the same time period as the postseismic interferograms (12/13 April 2010 – 1 July 2010) in the southwestern half of the Imperial Valley. Uncertainties in the line-of-sight measurement of the UAVSAR instrument, coupled with the sparseness of the GPS network, did not permit the decomposition the UAVSAR observations into horizontal and vertical deformation. However, the GPS and UAVSAR data were combined in the following inversions and in the interpretation of the data.

We compared the UAVSAR line of site measurements to GPS results calculated for the same time frame as the UAVSAR data (Figures 3 and 4). We converted the GPS north, east, and up vectors to line of site for the given azimuth and elevation for that location in the swath. UAVSAR pixels were averaged over a 1x1 km box. The results show that for local scales the correlation between the UAVSAR and GPS results is good and that the UAVSAR results can be deemed reliable. Ramps in the solution and other effects make it difficult to draw more regional conclusions from the UAVSAR solutions. GPS results can be used to validate and presumably improve the UAVSAR results over time. Unfortunately there are no GPS stations located in the western lobe of the interferogram to provide constraints on the results there.

The GPS data indicate coseismic uplift during the event [Wei et al, 2011], but also show a trend of uplift for the period 21 October 2009 – 13 April 2010 (Figure 2A). A similar pattern of uplift is observed in the postseismic GPS solution, but is more confined to the southern and western Imperial Valley (Figure 2C). If the uplift were observed only for the time of the El Mayor – Cucupah earthquake it is possible that liquefaction caused local uplift of the GPS monuments [Sasaki and Tamura, 2004]. Instead there seems to be a persistent broad pattern of regional uplift.

Webb et al. [2009] and Kedar [written communication] calculated time dependent strain for southern California based on continuous GPS measurements. Their results show substantial dilatation across the Imperial Valley in the region between the Salton Sea and the Mexican border, which grows more pronounced before the El Mayor-Cucapah earthquake. A ring of compression surrounds the Imperial Valley during this time period. More dilation is observed coseismically with compression at the edges, suggesting a regional dome of uplift associated with the earthquake similar to the elliptical pattern observed in the interferograms.

The coseismic interferogram on line 26501 includes the timespan April 12–13, 2010, whereas line 26505 does not. A two lobed pattern of deformation is observed in the April 12–13, 2010 timeframe (Figure 2B, suggesting that rapid postseismic motions occurred in the weeks following the event. This two lobed pattern continues for the April 13 – July 1, 2010 timeframe (Figure 2C) and is suggested in the July 1 – December 1, 2010 interferogram (Figure 2D). Two conjugate zones of shear are observed during this longer postseismic time period.

We plotted the line of site range changes for these three time periods on four transects. The first two transects (Lines A and B) are oriented perpendicular to the strike of the mainshock rupture with line A being further north and further away from the northern extent of the rupture. Line B spans the interferogram along and just north of the Yuha fault. Line C runs parallel to and just north of the extension of the mainshock rupture and crosses the Yuha fault. Line CC runs north-south through the east lobe and maximum displacement present in the interferogram. Line D crosses north-south perpendicular to the fringes on the eastern side of the Imperial Valley.

We converted the GPS deformation measurements into line-of-sight motions commensurate with the UAVSAR observation geometry of the interferograms. The elevation between the ground and the instrument varies from about 20° at the far edge of the swath to about 65° at the near edge of the swath for UAVSAR relative to the instrument. We used an elevation angle that matched or was most appropriate to the closest UAVSAR observation (pixel) and an azimuth of -5°, which is perpendicular to the flight path heading of the aircraft. As a result, GPS projections can vary according to the swath on which they were projected. The locations of the GPS stations do not lie on the cross section line for the most part, so we projected the locations of the GPS stations onto nearby lines (Figures 3–6). Some of the GPS stations are far from the lines, but still provide a general validation of the observed InSAR products. There can be an unknown overall phase constant in the interferogram that must be constrained with knowledge of areas known not to be undergoing deformation or with in situ measurement from GPS. We corrected the UAVSAR range change by a constant offset for the entire image to match the GPS range change estimates for stations on or very near the lines.

The coseismic observations indicate about 4 cm of coseismic change near the rupture (Figure 2A). The interferogram shows a fabric of conjugate northeast and northwest striking surface ruptures (Figure 7A). In our convention, positive range change is toward the aircraft. The GPS stations roughly indicate the same sense of motion as the UAVSAR data. Line B, which is closer to the rupture shows about 10 cm of motion peak to peak. The region between stations P494 and P496 shows a noisy but much flatter profile of motion. This is an indication of liquefaction, causing leveling at the western edge of the Imperial Valley on approximately a 10 km scale. The postseismic Lines A and B for the period 13 April – 1 July 2010 suggests the development of a fault stepover indicating continued activity at the northern end of the rupture. 3 cm of right slip are observed on the northwest stepover in the time period 13 April – 1 July 2010 and about 5 cm of range change are observed at the northern extension of the mainshock rupture. A ramp in the data is likely due to unmodeled errors. Line C shows a range change difference of over 30 cm from the north edge of line 26501 through the northeast lobe of the interferogram and offsets on the Yuha fault and a fault to the south coseismically and postseismically (Figure 4). Line CC shows a 60 cm gradient across the main or eastern lobe of the interferogram (Figure 5), which is due to a large slip gradient near the north end of the rupture.

Further east the coseismic and UAVSAR data show much greater variations along profile line D (Figure 6). Water in the region leading to mechanical instability along with liquefaction most likely disturbed the area during the event, but can also result in soil moisture changes and an additional source of error in the UAVSAR solutions. The GPS results show small postseismic motions and the excursion seen in the UAVSAR postseismic observations are most likely due to unmodeled errors.

Co- and Postseismic Fault Slip

The combined GPS and UAVSAR data, which include one week of postseismic motion, can be inverted for a single fault (Table 2). The inversions use three surface displacement components at GPS station locations, and one displacement component (in the illumination direction) at UAVSAR-observed pixel locations, with surface displacements calculated by elastic half-space dislocations [Okada, 1985]. Inversion is carried out by a residual-minimization procedure [Donnellan and Lyzenga, 1998], estimating the geometry and slip of one or more uniformly-slipping rectangular fault patches. Wei et al [2011] fit a model of a similar 120 km rupture to spaceborne radar data that observe the rupture and GPS data, but use seismicity to constrain the model to two long faults offset by a normal fault, and a fault segment at the north end of the rupture. We used the Wei et al [2011] four segment and multiple fault patch model, but the resulting surface deformation did not vary much north of the rupture. An average slip works approximately as well. These models produce a general gradient across the region of the interferogram, that must be taken into account, but do not contribute much to understanding the local slip. The north end of the rupture in our inversion is about 3 km north of the mapped rupture, suggesting some combination of deeper slip that did not rupture the surface in this region, or northward migration of slip during the immediate postseismic period.

The interferogram of the El Mayor-Cucapah earthquake shows linear northeast striking patterns that cross and offset the fringes (Figure 7). The most prominent of these is on the Yuha fault, which is a northeast trending strike-slip fault just north of the border between California and Baja [Treiman, 2011]. There is indication in the interferogram of a smaller secondary fault further south that we do not model here. The northeast striking lineations can be fit by a single fault at depth that is sub-parallel to, but south of, the

Yuha fault. The results suggest superficial slip on the Yuha and secondary fault in the unconsolidated surface sediment, but a simpler pattern of slip on a single fault at depth.

A map view of the interferogram in the region of the mainshock suggests that a stepover develops following the earthquake. Modeling suggests that the El Mayor-Cucupah rupture is bounded on the north by the left-lateral northeast striking, Yuha fault (Figure 9). These faults continued to slip to December 1, 2010 (Figures 7B–D). On 15 June 2010 a M 5.7 aftershock occurred just northwest of the northern terminus of the rupture. The epicenter of the event is proximal to the linear discontinuity in the postseismic interferogram and the mechanism of the event is consistent with slip on this stepover.

Inversions for slip on the northeast linear structure that steps west of the mainshock rupture yield a moment magnitude ranging from 5.5 – 5.8 (Table 3), which is consistent with the magnitude of the aftershock. We carried out inversions for one, two, and three fault segments for the observed postseismic interferogram. The χ^2/dof of the best-fit model is 0.47 and includes slip on the two offset northwest striking faults separated by the left-lateral Yuha fault. The χ^2/dof for a single fault is 1.54, or three times worse than the three fault segment model. While even the 3-fault model does not exhaust the data (it accounts for 73% of the variance in the radar image, leaving additional evidence of fault slip in the residuals), the UAVSAR data point to locations of the structures, their stepovers, and conjugate structures with the Yuha fault being the primary conjugate structure. The close proximity of the faults superposed gradients on the surface deformation from slip on the other faults. As a result, slip on the three structures best accounts for all of the observed deformation. We carried out numerous models leaving various parameters free and fixed, which helped us to converge on the models presented here. For the postseismic models presented here we fixed the location, strike, and length of the fault surfaces based on those identified in the UAVSAR image. An eastward dip is preferred on the northeast striking faults. Cumulatively the moment release from the earthquake to 1 July 2010 is equivalent to M 6.0.

While the model cannot provide exact details of postseismic rupture characteristics, we found that numerous model runs indicate that the main shock rupture terminates at the Yuha fault. Afterslip on the main shock is required by the models. Left slip occurs on the conjugate Yuha fault. Deeper slip is associated with the 15 June 2010 Coyote Creek aftershock. The models prefer a steeply dipping fault, with dip slightly eastward and slip at a depths of 2-10 km. We explored the relocated earthquakes of Hauksson et al [2011] and found that the earthquakes from 2–8 km in that region fall on a plane that follows the stepover imaged by UAVSAR. A cross section by depth through that line suggests a slight eastward dip. The deep and shallow locations are much more diffuse.

Coseismic creep is observed on the Superstition and Imperial faults (Figure 10). Using the assumption that all of the slip is horizontal, and parallel to the respective fault, 2 cm of horizontal right-lateral slip occurred on the Superstition Hills fault, and 4 cm of right-lateral strike slip motion occurred on the Imperial fault. These results show that locally UAVSAR can produce very detailed observations of surface deformation and provide good indicators of the depth of slip.

Observed Uplift in the Imperial Valley

The UAVSAR observations suggest a dome of vertical deformation in the Imperial Valley. However, the horizontal motions overwhelm the results in the repeat pass interferogram, making it difficult to infer any pattern of vertical motions. GPS results for the region indicate about 2 cm of uplift in the Imperial Valley associated with the earthquake and subsidence near and west of the rupture. Additional uplift of about 7 mm in the southerwestern half of the Imperial Valley occurred between the time of the earthquake and 1 July 2010 (Figure 2).

Over the longer term, since the earthquake, the stations closest to the northeast end of the co-seimic rupture show the most uplift. Station P494 subsided following the earthquake and then rose about 30 mm in the 1 April 2011 – 28 July 2011 time frame (Figure 11). Station P496 showed a uniform rate of uplift, amounting to about 20 mm in the time frame from the earthquake on 10 April 2010 to 28 July 2011. Water or magma injection could explain the Imperial Valley pattern of uplift. The southeastward motion of the eastern side of the fault rupture would cause a pull apart in the Imperial Valley, consistent with the dilation that is calculated from the GPS time series data [Webb et al, 2009] and well developed rifting [Swanberg, 1982].

We compare the Yellowstone caldera to the Salton Trough to explain the vertical motions. At a very simplistic level, the Yellowstone caldera region and the Salton trough have several interesting features in common: both experience frequent large earthquakes, both have very high heat flow, and associated geysers and/or mud volcanoes. There have been several episodes of inflation and deflation of the Yellowstone caldera floor in the period of time covered by annual leveling surveys starting in 1976. Many of the episodes of vertical motion were associated in time with earthquake swarms and changes in activity of geysers and mud pots [Dzurisin, 2007]. There have been several large historic earthquakes in the region with the largest being the M 7.5 Hebgen Lake event on 18 August 1959.

The long-term (10^5 to 10^6 year) source of both high heat flow and elevated topography is "episodic intrusion of new basaltic magma from the mantle into the crust beneath the caldera" [Dzurisin, 2007, p. 254]. There is good evidence for a partly molten rhyolitic magma at depth [Christiansen, 2001; Smith and Braile, 1994].

A leveling survey of the Yellowstone caldera was conducted in 1923 and then from 1976 onward. The survey has been repeated on a yearly basis. Starting in 1990, these leveling surveys have been supplemented by GPS measurements, which also measure both vertical and horizontal motion. Starting in 1992 InSAR measurements have also been obtained. These surveys show several episodes of inflation and subsidence of the caldera floor [Dzurisn and Yamashita, 1987; Dzurisin et al., 1990]. The caldera rim has remained relatively stable, but the center showed 90 cm of uplift from 1923 to 1985, followed by 20 cm of subsidence between 1985 and 1995, followed by uplift since 1995. The rate of uplift increased dramatically in 2004 [Chang et al., 2007], and has continued until the present, though not at the 5-7 cm/yr rate seen between 2004 and 2006 [Chang et al., 2010]. The likely mechanisms for short term vertical motion include both movement of magma [Christiansen, 2001; Smith and Braile, 1994] and pressurization of the deep hydrothermal system [Fournier, 1989, Dzurisin et al., 1990].

Fournier and Pitt [1985] proposed that the Yellowstone hydrothermal system has a deep zone in which pore fluid pressure is near lithostatic, and a shallow zone in which pore pressure is hydrostatic. The two zones are presumed to be separated by an impermeable, self-sealing layer created by mineral deposition and plastic flow at a depth near 5 km. In this model, uplift can be explained by water released upon crystallization of rhyolitic magma. The net volume increase would yield surface uplift [Fournier, 1989; Dzurisin et al., 1990]. If the self-sealed layer within the deep hydrothermal system were ruptured during an earthquake swarm, the resulting depressurization and fluid loss would lead to surface subsidence.

It is tempting to draw parallels between behavior seen in Yellowstone and that in the Salton Trough. There are obvious similarities, including high heat flow, recent volcanic activity, and occasional large earthquakes. Rudolph and Manga [2010] observed an increase in gas flux from mud volcanoes near to the location of the 4 April 2010 El Mayor-Cucapah earthquake, and argued that it was due to a transient increase in subsurface permeability.

In addition to the 5 small rhyolite domes, which were extruded onto the Quaternary sediments at the south end of the Salton Sea [Robinson et al., 1976], it has recently been found that there are thick (150-300 m) rhyolite layers at 1.6 to 2.7 km depth in the same area [Schmitt and Hulen., 2008]. They appear to have been emplaced roughly 400 kyr ago. Assuming that the sedimentation rate roughly equals the subsidence rate [Lachenbruch et al., 1985], this implies a mean subsidence rate of 4-6 mm/yr, which is close to the estimate from repeat leveling [Larsen and Reilinger, 1991]. However, trenching across the Brawley fault zone [Meltzner et al., 2006] has shown that the recent sedimentation rate from 1970 to 2004 was at least twice as fast as the average over the preceding millennium.

Holocene eruptions at the south end of the Salton Sea as recent at 16,000 years ago and hydrothermal activity suggest that magma in the region is at a shallow depth

[Goldstein and Flexser, 1984]. Other studies indicate a magma chamber at 5 km depth with magma that can be as shallow as 1.5 km [Robinson et al, 1976]. Robinson et al [1976] suggest that this region is a leaky transform fault. Swanberg [1983] suggests that free convection may be occurring and Rex et al [1982] suggest a large geothermal field underlying the Salton Trough at depths greater than 4 km with temperatures greater than 400°C. These could be factors contributing to the observed regional pattern of uplift. Chang et al [2007] suggest that a large deep expanding volcanic sill can explain the regional uplift pattern in Yellowstone. A similar mechanism may be occurring in the Salton Trough.

Conclusions

The El Mayor – Cucupah earthquake triggered slip on several right-lateral and conjugate left-lateral faults in the Salton Trough (Figure 12). The stepover observed in the UAVSAR data connects the Laguna Salada and Elsinore faults. The left-lateral Yuha fault bounds the northern end of the 2010 rupture and the southern end of the westward-displaced left stepover. The broad pattern of uplift suggests a regional intrusion of water or possibly magma. The region of uplifting crust localizes southwestward over the year following the earthquake. The observed pattern of coseismic and postseismic deformation induced by the 2010 El Mayor-Cucapah earthquake is consistent with the transitional tectonic regime, and the historic record of earthquake sequences in which major events have occurred on northwest-trending strike-slip faults, and with minor slip on conjugate cross-faults. The history of triggered slip and sequences of earthquakes suggests the potential for triggering an earthquake on the southern Elsinore fault zone, which has not ruptured in several centuries.

Acknowledgements

This work was carried out at the Jet Propulsion Laboratory, California Institute of Technology under contract with NASA. We thank Michael Heflin and Geoffrey Blewitt for useful discussion and additional analysis of GPS data. QuakeSim tools and the QuakeSim computational environment were used extensively in the analysis and modeling presented here.

References

Blisniuk, K, Rockwell, T., Owen, L. A., Oskin, M., Lippincott, C., Caffee, M. W., and Dortch, J., (2010), Late Quaternary slip rate gradient defined using high-resolution topography and 10Be dating of offset landforms on the southern San Jacinto FAult zone, California: *J. Geophys Res.*, v. 115, B08401, doi:10.1029/2009JB006346.

Chang, W-L., R.B. Smith, C.Wicks, J.M. Farrell, C.M. Puskas (2007), Accelerated Uplift and Magmatic Intrusion of the Yellowstone Caldera, 2004 to 2006, Science, 318, 952-956, *DOI:* 10.1126/science.1146842.

Chang, W-L., R.B. Smith, J.M. Farrell, C.M. Puskas (2010), An extraordinary episode of Yellowstone caldera uplift, 2004–2010, from GPS and InSAR observations, Geophys. Res. Lett., 37, L23302, doi:10.1029/2010GL045451.

Christiansen, R.L., (2001), The Quaternary and Pliocene Yellowstone Plateau volcanic field of Wyoming, Idaho, and Montana: U.S. Geological Survey Professional Paper 729-G, 144 p. *http://pubs.usgs.gov/pp/pp729g/*.

Donnellan, A., and Lyzenga, G.A. ,(1998), GPS observations of fault afterslip and upper crustal deformation following the Northridge earthquake, J. Geophys. Res., 103,21,285-21297.

Dzurisin, D., and Yamashita, K. M. (1987), Vertical surface displacements at Yellowstone caldera, Wyoming: Journal of Geophysical Research, v. 92, no. B13, p. 13,753-713,766.

Dzurisin, D., Savage, J. C., and Fournier, R. O. (1990), Recent crustal subsidence at Yellowstone caldera, Wyoming, Bull. Volcan., 52, 247-270.

Dzurisin, D., K.M. Yamashita, and J.W. Kleinman (1994), Mechanisms of crustal uplift and subsidence at the Yellowstone Caldera, Wyoming, Bull. Volcan., 56,261-270.

Fay, N. P., and E. D. Humphreys (2005), Fault slip rates, effects of elastic heterogeneity on geodetic data, and the strength of the lower crust in the Salton Trough region, southern California, J. Geophys. Res., 110(B9), B09401, doi:10.1029/2004JB003548.

Fournier, R.O., and A.M. Pitt (1985), The Yellowstone magmatic hydrothermal system, in C. Stone (ed) Geothermal Resources Council 1985 International Symposium on Geothermal Energy, pp. 319-327.

Fournier, R. O. (1989), Geochemistry and dynamics of the Yellowstone National Park hydrothermal system: Annual Reviews of Earth and Planetary Sciences, v. 17, p. 13-53.

Goldstein, N.E., S. Flexser (1984), Melt Zones Beneath Five Volcanic Complexes in California: An Assessment of Shallow Magma Occurrence, Lawrence Berkeley Laboratory Report LBL-18232.

Hauksson, E., J. Stock, K. Hutton, W. Yang, A. Vidal-Villegas, H. Kanamori (2010), The 2010 M_w 7.2 El Mayor-Cucapah Earthquake Sequence, Baja California, Mexico and Southernmost California, USA: Active Seismotectonics along the Mexican Pacific Margin, Pure and Applied Geophysics, DOI 10.1007/s00024-010-029-7.

Hauksson, E., W. Yang, and P. Shearer (2011), "Waveform Relocated Earthquake Catalog for Southern California (1981 to 2011)," 2011 SCEC Annual Meeting Abstract, Palm Springs.

Hensley, S., T. Michel, M. Simard, C. Jones, R. Muellerschoen, C. Le, H. Zebker, and B. Chapman (2008), Residual motion estimation for uavsar: Implications of an electronically scanned array, Proc. of Radarcon 2008.

Hill, D. P., Eaton, J. P. and Jones, L. M. (1990), Seismicity, 1980-86, in "The San Andreas Fault System, California", *USGS Prof. Paper* 1515.

Holliday, J.R., C.C. Chien, K.F. Tiampo, J.B. Rundle, D.L. Turcotte, and A. Donnellan (2007), A RELM Earthquake Forecast Based on Pattern Informatics, Seismological Research Letters, 78:1, 87–93.

Hudnut, K., Seeber, L., Rockwell, T., Goodmacher, J., Klinger, R., Lindvall, S. and McElwain, R. (1989), Surface ruptures on cross-faults in the 24 November 1987 Superstition Hills, California, earthquake sequence, *Bull. Seismol. Soc. Amer.,* v 79, 330-341.

Irwin, W. P. (1990), Geology and Plate-Tectonic Development, in "The San Andreas Fault System, California", *USGS Prof. Paper* 1515.

Lachenbruch, A.H., J.H. Sass, S.P. Galanis Jr. (1985), Heat Flow in Southernmost California and the Origin of the Salton Trough, J. Geophys. Res., 90, 6709-6737, doi:10.1029/JB090iB08p06709.

Larsen, S., and R. Reilinger (1991), Age Constraints for the Present Fault Configuration in the Imperial Valley, California, Evidence for Northwestward Propagation of the Gulf of California Rift System, J. Geophys. Res., 96, 10,339-10,346.

Lee, Y-T, D.L. Turcotte, J.R. Holliday, J.B. Rundle, C-C. Chen, K.F Tiampo (2011), Results of the RELM test of earthquake predictions in California, submitted to Proc. Nat. Acad. Sci.

McCrink, T.P., Pridmore, C.L., Tinsley, J.C., Sickler, R.R., Brandenberg, S.J., and Stewart, J.P. (2011), Liquefaction and other ground failures in Imperial County, California, from the April 4, 2010, El Mayor- Cucapah earthquake: U.S. Geological Survey Open-File Report 2011-1071 and California Geological Survey Special Report 220, 94 p. pamphlet, 1 pl., scale 1:51,440. [http://pubs.usgs.gov/of/2011/1071/] [http://conservation.ca.gov/cgs] Version 1.0.

Meade, B.J., and B.H. Hager (2005), Spatial localization of moment deficits in southern California, J. Geophys. Res., B04402, doi:10.1029/2004JB003331.

Meltzner, A.J., T.K. Rockwell, L.A. Owen (2006), Recent and Long-Term Behavior of the Brawley Fault Zone, Imperial Valley, California: An Escalation in Slip Rate?, Bull. Seism. Soc. Am., 96, 2304-2328, DOI: 10.1785/0120050233.

Millman, D.E., and Rockwell, T.K., 1986, Neotectonics of the Elsinore fault in Temescal Valley, California, *in* Ehlig, P.L., complier, Neotectonics and faulting in southern California (Geological Society of America 82nd Annua Meeting Guidebook): Los Angeles, California State University, p. 159–166.

Moore, A. W., S. Kedar, F. Webb, Z. Liu, Y. Bock, P. Fang, Evaluation of Tropospheric Zenith Delays Estimated from GPS Data and Derived from Weather Model Weather Vapor Data, in the Context of InSAR Tropospheric correction, Abstract G53B-0725 presented at 2010 Fall Meeting, AGU, San Francisco, Calif., 13-17 Dec. 2010.

Nicholson, C., Seeber, L., Williams, P. and Sykes, L. R. (1986), Seismic evidence for conjugate slip and block rotation within the San Andreas fault system, southern California, *Tectonics*, v. 5, no. 4, p. 629-648 (1986). Robinson, P.T., Elders, W.A., and Muffler, L.J.P., Quaternary volcanism in the Salton Sea geothermal field, Imperial Valley, California. Geol. SOC. Am. Bull., V . 87, pp. 347-360.

Okada, Y (1983)., Surface deformation due to shear and tensile faults in a half-space, Bull. Seim. Soc. Am., 75, 1135-1154.

Rex, R.W. (1982), Hidden elephants under our noses, Geotherm. Res. Counc. Bull., 11: 13-15.

Robinson, P.T., W.E. Elders, L.J.P. Muffler (1976), Quaternary volcanism in the Salton Sea geothermal field, Imperial Valley, California, Geol. Soc. Am. Bull., 87, 347-360, DOI: 10.1130/0016-7606(1976)87<347:QVITSS>2.0.CO;2.

Rockwell, T., C.Loughman, P. Merifield (1990), Late Quaternary Rate of Slip Along the San Jacinto Fault Zone Near Anza, Southern California, J. Geophys. Res., 95, 8593-8605, doi:10.1029/JB095iB06p08593.

Rudolph, M.L., and M. Manga (2010), Mud volcano response to the 4 April 2010 El Mayor-Cucapah earthquake, J. Geophys. Res., 115 , B12211, doi:10.1029/2010JB007737.

Rundle, J.B., K.F. Tiampo, W. Klein and J.S.S. Martins (2002), Self-organization in leaky threshold systems: The influence of near mean field dynamics and its implications for earthquakes, neurobiology and forecasting, *Proc. Nat. Acad. Sci*. USA, **99**, Supplement 1, 2514-2521.

Rundle, JB, DL Turcotte, C Sammis, W Klein and R. Shcherbakov (2003), Statistical physics approach to understanding the multiscale dynamics of earthquake fault systems (invited), *Rev. Geophys. Space Phys*., **41**(4), DOI 10.1029/2003RG000135.

Sasaki, T. and K. Tamura (2004), Prediction of Liquefaction-Induced Uplift Displacement of Underground Structures, 36th Joint Meeting Panel on Wind and Seismic Effects, Gaithersburg, Maryland, 17-22 May.

Schmitt, A.K., J.B. Hulen (2008), Buried rhyolites within the active, high-temperature Salton Sea geothermal system, J. Volcanology and Geothermal Res., 178, 708-718.

Smith, R.B., and L.W. Braile (1994), The Yellowstone hotspot: Journal of Volcanology and Geothermal Research, v. 61, p. 121-187.

Swanberg, C.A. (1983), Geothermal Resources of Rifts: A Comparison of the Rio Grande Rift and the Salton Trough, Tectonophysics, 94, 659-678.

Tiampo, KF, JB Rundle, S. McGinnis, S. Gross and W. Klein (2002), Mean field threshold systems and phase dynamics: An application to earthquake fault systems, *Europhys. Lett.*, **60**, 481-487.

Toppozada, T. R., Branum, D. M., Reichle, M. S., and Hallstrom, C. L. (2002), San Andreas Fault Zone, California: M≥5.5 Earthquake history, *Bull. Seism. Soc. Amer.,* v. 92, no. 7, pp 2555-2601.

Treiman, J.A., 2011, Faults of the Yuha Desert and the southeastern portion of the Elsinore Fault Zone, Imperial County, California: California Geological Survey, Fault Evaluation Report FER-254, *in review*.

Webb, F., Y. Bock, S. Kedar, S.E. Owen, D. Dong, P. Jamason, P. Fang, M.B. Squibb, B.W. Crowell, D. Avraham (2009), Solid Earth Science Data System for Exploration of Lithospheric Deformation in the Western US, American Geophysical Union, Fall Meeting 2009, abstract #IN42A-07.

Wei, S., E. Fielding, S. Leprince, A. Sladen, J-P. Avouac, D. Helmberger, E.Hauksson, R. Chu, M. Simons, K. Hudnut, T. Herring, and R. Briggs (2011), Superficial simplicity of the 2010 El Mayor-Cucapah earthquake of Baja California, Mexico, Nature Geoscience, DOI:10.1038/NGEO1213.

Weldon, R.J., K.E., Sieh (1985), Holocene rate of slip and tentative recurrence interval for large earthquakes on the San Andreas fault, Cajon Pass, southern California, Geol. Soc. Am. Bull., doi: 10.1130/0016-7606(1985)96<793:HROSAT>2.0.CO;2, 96, 293-812.

WGCEP: Working Group of California Earthquake Probability (2007), *The Uniform California Earthquake Rupture Forecast, v2* (USGS Open File Report 2007-1437; http://pubs.usgs.gov/of/2007/1437/).

Figure Captions

Figure 1. Top Panel: Regional context of the UAVSAR study in the Salton Trough. The Pacific North American plate boundary is shown by the solid line, with general sense of motion marked by gray arrows. Seismicity is plotted for the time of the UAVSAR study, which is from October 20, 2009 – December 1, 2010. Area of study, GPS uplift and coseismic UAVSAR repeat pass interferometry images are also shown. Bottom Panel: region of study showing general Pacific-North American plate motion marked as darker gray arrows. Heavy dashed lines mark slip of the mainshock rupture and faults with observed creep. Arrows indicate general sense of motion. Red circles indicate GPS uplift and blue circles subsidence observed by GPS station.. Largest circle shows about 2 cm of uplift. Light dotted lines indicate sections along which UAVSAR line of sight (LOS) changes are plotted in subsequent figures. Northern swath is line 26505 and southern swath is line 26501.

Figure 2. L-band UAVSAR repeat pass interferometry (RPI) products. Each cycle through the color wheel indicates 12 cm of displacement along the radar line of sight. Dotted lines indicate sections along which UAVSAR line of sight (LOS) changes are plotted in subsequent figures. Lines A and B are roughly perpendicular to the mainshock fault motion, line C is perpendicular to the Yuha fault, CC passes through the maximum observed displacements, and Line D through the Imperial Valley. A) Coseismic unwrapped interferogram and vertical coseismic GPS observations for the time period October 2009 – April 2010. Timeframe for the northern swath, which is line 26505, is

October 20, 2009 – April 12, 2010. The southern swath is line 26501 and the time frame for first and second passes is October 21, 2009 – April 13, 2010. Red circles indicate uplift and blue circles indicate subsidence. Largest observed uplift is 2 cm and largest subsidence is -1.3 cm. B) Unwrapped interferogram for postseismic observations for the period April 12-13, 2010. C) Postseismic inteferogram for the time period April 13 – July 1, 2010. Linear offsets are marked by dotted ellipses. D) Postseismic interferogram for the time period July 1, 2010 – December 1, 2010.

Figure 3. UAVSAR line of site measurements versus GPS line of site component from 3D GPS solutions for the same time period. UAVSAR pixels are averaged over a 1x1 km box. GPS north, east, and up, are converted to line of site for the elevation and azimuth at each GPS point. Dotted line in each plot shows a correlation of 1. A) An offset of 10.02 cm is removed from UAVSAR by averaging differences between the GPS and UAVSAR line of site estimates. IID2 and P500 are removed from the first fit and fit separately. The offset between the two fits is 7 cm. B) An offset of 4.6 cm is added to the UAVSAR. Only P497 and P77 are in the first fit. The difference between GPS solutions is less than 2 cm while the variance in UAVSAR at those points is 7 cm. C) An offset of 1.2 cm is added to the UAVSAR. P500 is deleted from the first fit and the average. P500 is 8 cm different than the corresponding GPS observation. D) An offset of 15.12 cm is added to the UAVSAR. P492 is not included in the average or first correlation fit.

Figure 4. Graphical illustration of fits from Figure 3 ranging from good correlation with the GPS of less than 1 cm (green) to poor fits (red and purple). Panels correspond to plots in Figure 3.

Figure 5. Cross sections for Lines A and B. Line of site range changes are plotted along the lines for coseismic and postseismic observations. GPS data are projected onto the line of site for the appropriate elevation angle for that point in the image and are plotted twice if located in two swaths. The GPS data were used to correct the range change ambiguity in this and subsequent plots.

Figure 6. Line of site range change in cm is plotted along the section perpendicular to the Yuha fault found at 5 km in the section. GPS data are projected onto the line of site for the appropriate elevation angle for that point in the image. Slip on two left-lateral structures that are conjugate to the mainshock rupture, near 5 and 8 km in the section.

Figure 7. Line of site range change in cm is plotted along a north south section through the largest displacements found in the coseismic repeat pass interferometry. GPS data are projected onto the line of site for the appropriate elevation angle for that point in the image.

Figure 8. Line of site range changes are plotted along the lines for coseismic and postseismic observations for a cross section through the Imperial Valley plotted north to south showing deformation pattern on that region.

Figure 9. Detail of the north end of the rupture for A) the coseismic interval of October 21, 2009 – April 13, 2010, B) April 12 – 13, 2010, C) April 13, 2010 – July 1, 2010, and D) July 1, 2010 – December 1, 2010. Offsets associated with the mainshock and the M 5.7 June 15, 2010 aftershock and conjugate slip on the Yuha fault persist in the images.

Figure 10. Coseismic creep on the Superstition Hills and Imperial faults can be seen in the coseismic interferograms for line 26505 and in the agricultural area in 26501 (south line). Detailed cross sections are plotted for each fault indicating 1 cm of line of site changes on the Superstition Hills fault and 2.3 cm of line of site changes on the Imperial fault. This corresponds to 2.0 creep on the Superstition Hills fault and 4.3 cm of creep on the Imperial fault if the slip is horizontal and parallel to the slip lineation.

Figure 11. Vertical time series for stations in the southern Imperial Valley spanning the north end of the rupture. Station plots are organized roughly geographically. Horizontal axis is time and vertical axis is vertical position in mm. Solid vertical line marks the time of the earthquake. Dashed lines mark the beginning of the coseismic interferograms and the end of the postseismic interferograms respectively.

Figure 12. Mapped faults in the Salton trough (solid labeled lines) and areas of slip identified by UAVSAR (dashed lines).

Tables

Repeat Pass Interferometry Product **Description**	**Pass 1** **Pass 2**	**Aircraft Heading**
SanAnd_26505_09083-006_10027-005_0174d_s01_L090_02 Coseismic Imperial Valley	2009/10/20 2010/04/12	-95.35
SanAnd_26501_09083-010_10028-000_0174d_s01_L090_02 Coseismic along Mexican border	2009/10/20 2010/04/13	-95.33
SanAnd_26501_10027-001_10028-000_0001d_s01_L090_01 Immediate postseismic along border	2010/04/12 2010/04/13	-95.34
SanAnd_26501_10028-000_10057-100_0079d_s01_L090_01 Postseismic along border	2010/04/13 2010/07/01	-95.38
SanAnd_26501_10057-100_10084-000_0153d_s01_L090_01 Later postseismic along border	2010/07/01 2010/12/01	-95.38

Table 1. Repeat Pass Interferometry product identifiers, dates of passes, and aircraft heading, with a description of characteristics and location of the line.

Model	Single Fault	Two Faults	
		Rupture	Yuha Fault
Latitude	32.641234	32.632167	32.729903
Longitude	-115.752267	-115.748914	-115.740246
Strike	134.1	134.1	46
Dip	-63.29	-63	-90
Length (km)	120	120	8
Depth (km)	0	0	0
Width (km)	11.1	11.2	0.5
Strike slip (cm)	131	145	-8
Dip slip (cm)	94	87	0
Tensile slip (cm)	0.1	0	0
Moment (dyne/cm^2)	6.4×10^{26}	6.8×10^{26}	9.5×10^{22}
M_w	7.2	7.2	4.6
Cumulative M_w	7.2	7.2	
X^2/dof	3.5	3.5	

Table 2. Combined GPS and UAVSAR inversions for fault slip for a single fault model and for a primary fault and secondary conjugate fault. $\mathbf{X^2}$ is computed based on estimated formal error of GPS displacements for each component and station (for 156 stations; at favorable stations uncertainties are 0.05, 0.05, 0.16 cm for east, north, and vertical, respectively) and a reduced set of 20,984 UAVSAR pixels assigned uncertainty of 1 cm. Observation uncertainties are treated as if uncorrelated. Fault latitude and longitude correspond to the NW end main rupture fault. The latitude and longitude of the Yuha fault corresponds to the SW corner of the fault. The depth of the fault corresponds to the top edge and a negative dip is downward to the NE for the mainshock rupture and vertical for the Yuha fault. In the final inversion reported in the table for the single fault model

the depth, width, and all slip parameters were left free. For the two fault model the location, strike-slip, and dip-slip of the rupture were left free and the width and slip on the Yuha fault were left free. Other parameters were left free in earlier runs to minimize the residuals.

Model	Single Fault	Two Faults		Three Faults		
	Aftershock	**Aftershock**	**Yuha Fault**	**Aftershock**	**Rupture**	**Yuha Fault**
Latitude	32.763021		32.645506	32.763021	32.667297	
Longitude	-116.000034		-115.822435	-116.000034	-115.805105	
Strike	128	128	36	128	128	36
Dip	-83	-83	-90	-83	-83	-90
Length (km)	18	20	9	18	25	6
Depth (km)	2	2	1	2	2	.4
Width (km)	10	10	9	10	10	9
Strike slip (cm)	4	6.5	-4.2	9.6	6.4	-7.6
Dip slip (cm)	1	1	0	1	0	0
Tensile slip (cm)	0	0	0	0	0	0
Moment (dyne/cm^2)	$2.2X10^{24}$	$3.9x10^{24}$	$1x10^{24}$	$5.2x10^{24}$	$4.8x10^{24}$	$1.2x10^{24}$
M_w	5.5	5.7	5.3	5.8	5.8	5.4
Cumulative M_w	5.5	5.8		6.0		
X^2/dof	1.54	1.2		0.47		

Table 3. UAVSAR inversions for postseismic motions. Fault latitude and longitude correspond to the NW ends of the afterhock and main rupture fault. The latitude and longidude of the Yuha fault corresponds to the SW corner of the fault. The depth of the fault corresponds to the top edge and a negative dip is downward to the NE for the aftershock and mainshock rupture and vertical for the Yuha fault. Strike slip is the only free parameter in the final inversion reported in the table, though other parameters were left free in earlier runs to minimize the residuals.

Figures

Figure 1

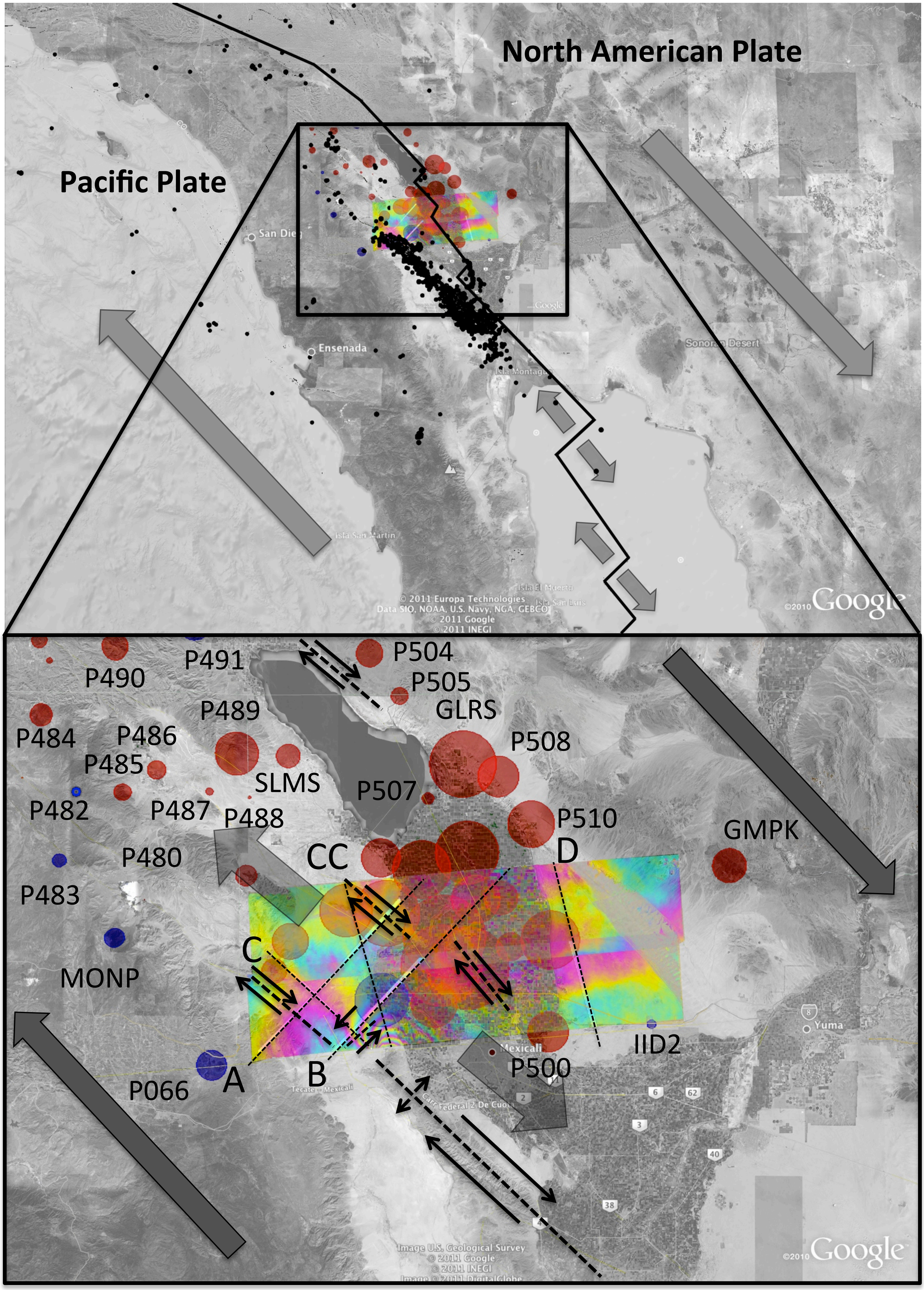

North American Plate
Pacific Plate
San Dieg
Ensenada
Sonoran Desert
Isla Montague
Isla San Martin
Isla El Muerto
Isla San Luis
© 2011 Europa Technologies
Data SIO, NOAA, U.S. Navy, NGA, GEBCO
© 2011 Google
© 2011 INEGI
©2010 Google
P491
P504
P505
P490
GLRS
P489
P484
P486
P508
P485
SLMS
P507
P482
P487
P488
P510
GMPK
P480
CC
D
P483
C
MONP
Yuma
Mexicali
IID2
P500
P066
A
B
Tecate
Carr Federal 2 De Cuo
Image U.S. Geological Survey
© 2011 Google
© 2011 INEGI
Image © 2011 DigitalGlobe
©2010 Google

Figure 2

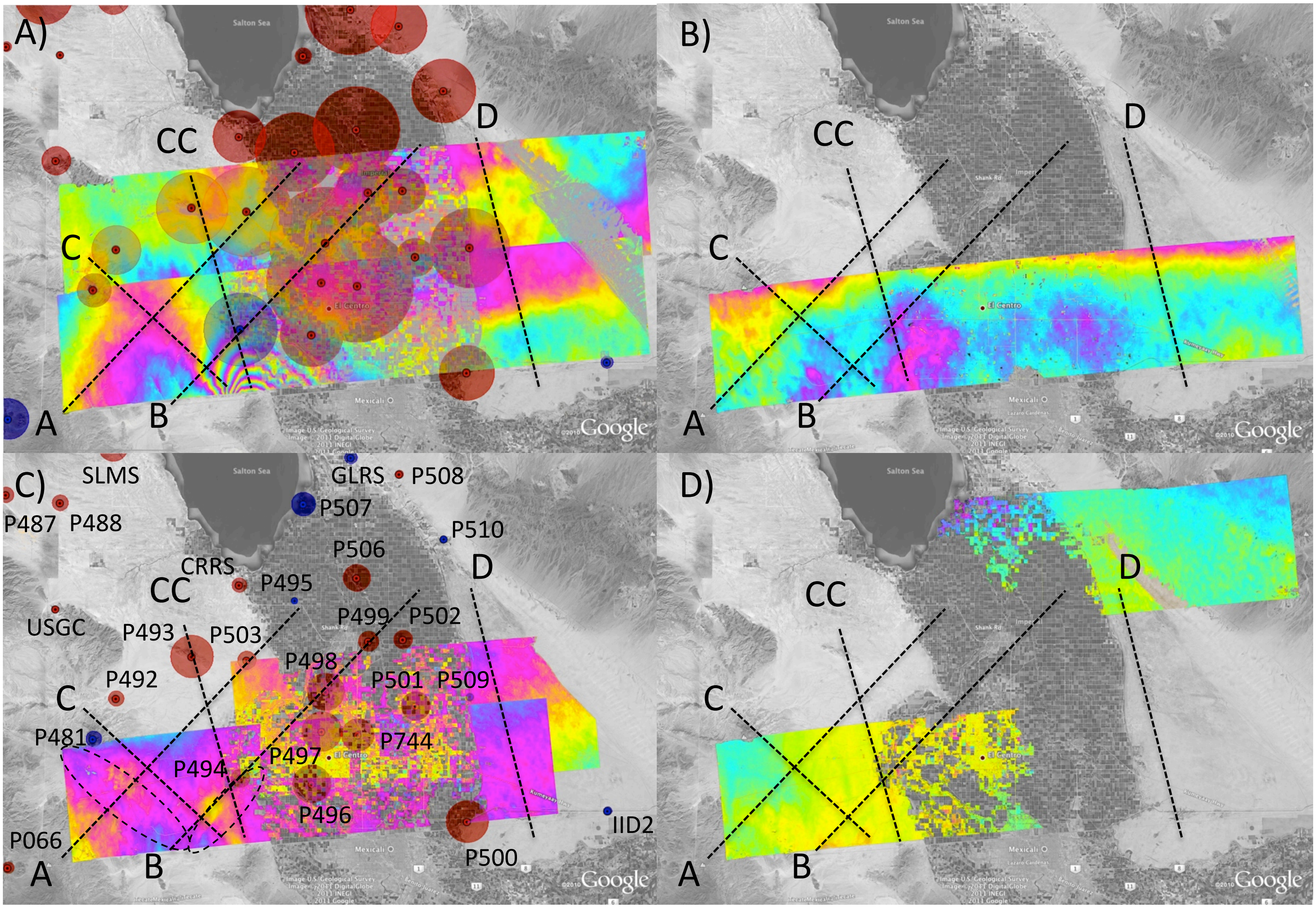

A)
CC
C
D
A
B
B)
CC
C
D
A
B
C)
SLMS
GLRS
P508
P487
P488
P507
P510
P506
CRRS
CC
P495
D
USGC
P493
P503
P499
P502
P498
P492
P501
P509
C
P481
P744
P494
P497
P496
P066
IID2
A
B
P500
D)
CC
D
C
A
B

Figure 3

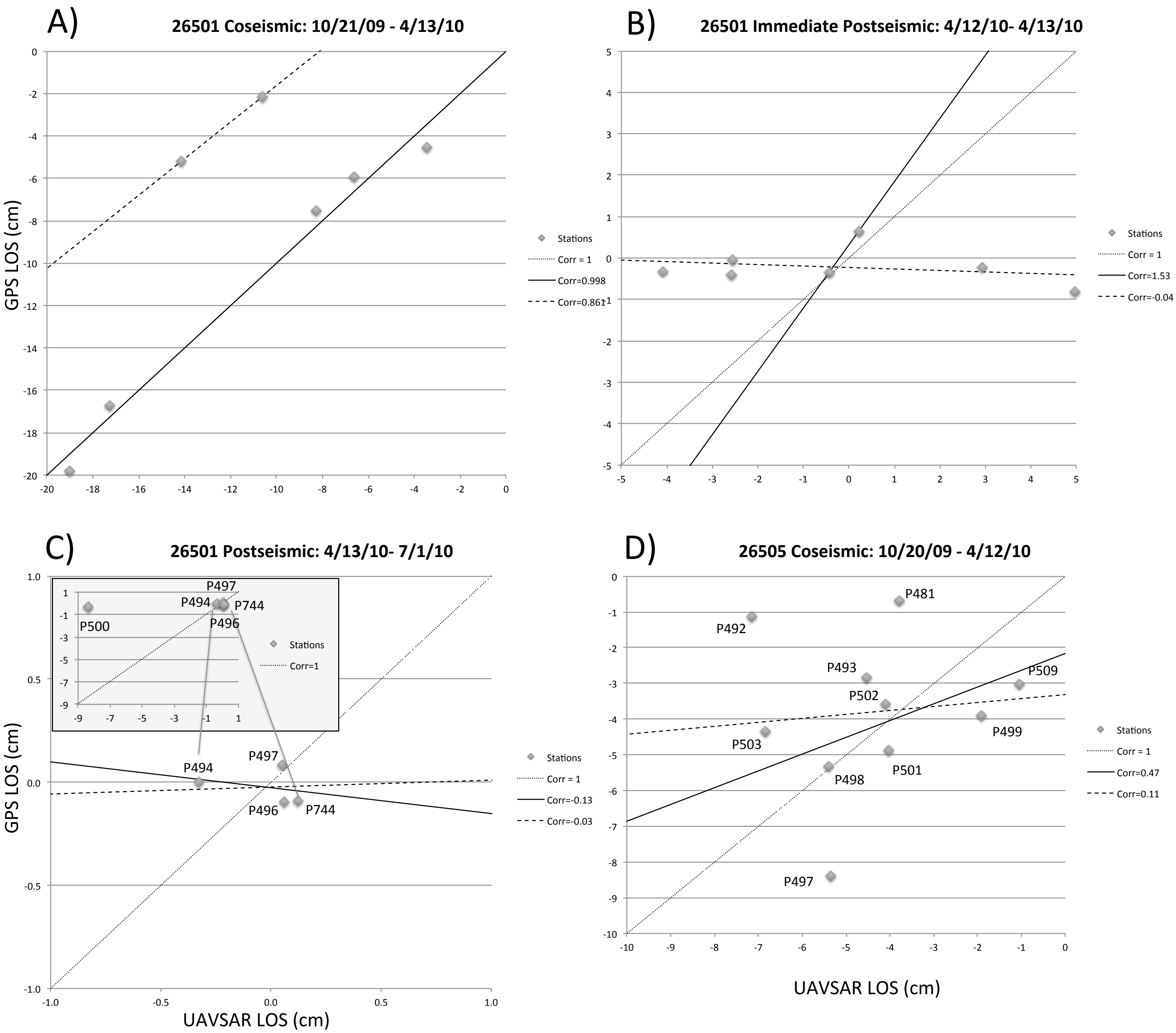
A)
26501 Coseismic: 10/21/09 - 4/13/10
GPS LOS (cm)
Stations
Corr = 1
Corr=0.998
Corr=0.861
B)
26501 Immediate Postseismic: 4/12/10- 4/13/10
Stations
Corr = 1
Corr=1.53
Corr=-0.04
C)
26501 Postseismic: 4/13/10- 7/1/10
P497
P494
P744
P496
P500
Stations
Corr=1
P497
P494
P496
P744
Stations
Corr = 1
Corr=-0.13
Corr=-0.03
GPS LOS (cm)
UAVSAR LOS (cm)
D)
26505 Coseismic: 10/20/09 - 4/12/10
P481
P492
P493
P509
P502
P499
P503
P501
P498
P497
Stations
Corr = 1
Corr=0.47
Corr=0.11
UAVSAR LOS (cm)

Figure 4

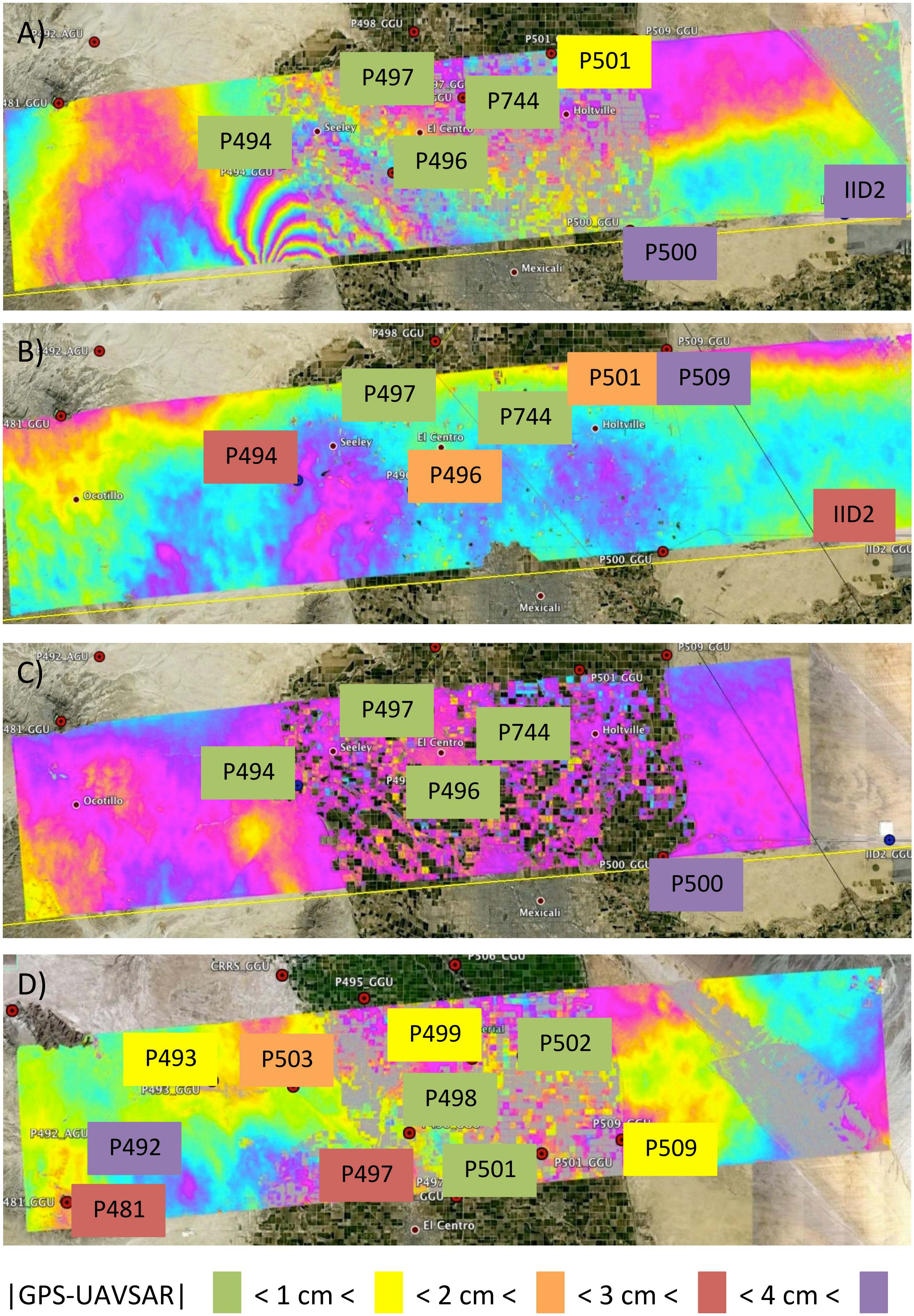
A)
P497
P501
P744
P494
P496
IID2
P500
Seeley
El Centro
Holtville
Mexicali
B)
P497
P501
P509
P744
P494
P496
IID2
Ocotillo
Seeley
El Centro
Holtville
Mexicali
C)
P497
P744
P494
P496
P500
Ocotillo
Seeley
El Centro
Holtville
Mexicali
D)
P493
P503
P499
P502
P498
P492
P509
P497
P501
P481
El Centro
|GPS-UAVSAR|
< 1 cm <
< 2 cm <
< 3 cm <
< 4 cm <

Figure 5

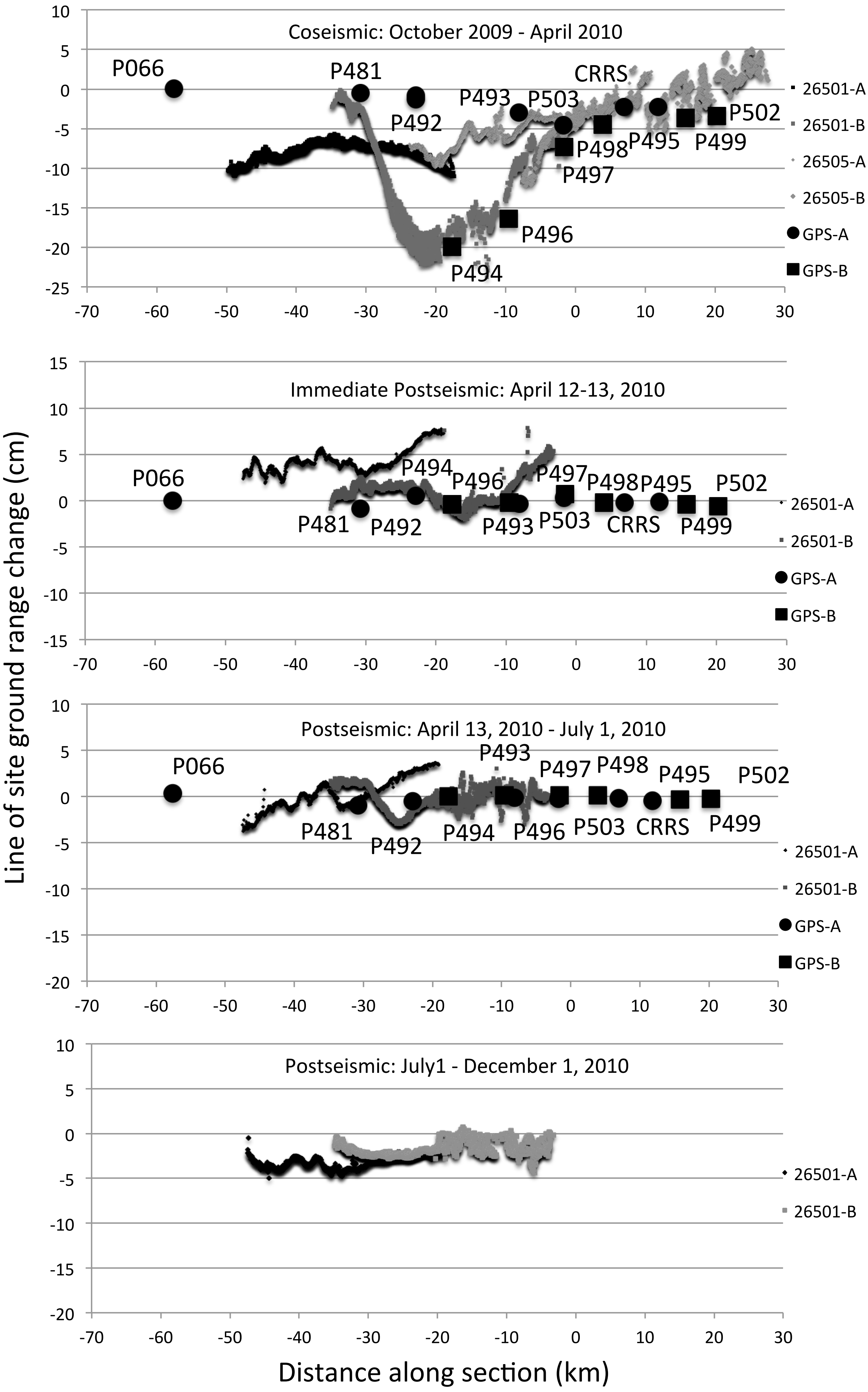
Coseismic: October 2009 - April 2010
P066
P481
P492
P493
P503
CRRS
P495
P502
P498
P499
P497
P496
P494
26501-A
26501-B
26505-A
26505-B
GPS-A
GPS-B
Immediate Postseismic: April 12-13, 2010
Postseismic: April 13, 2010 - July 1, 2010
Postseismic: July1 - December 1, 2010
Line of site ground range change (cm)
Distance along section (km)

Figure 6

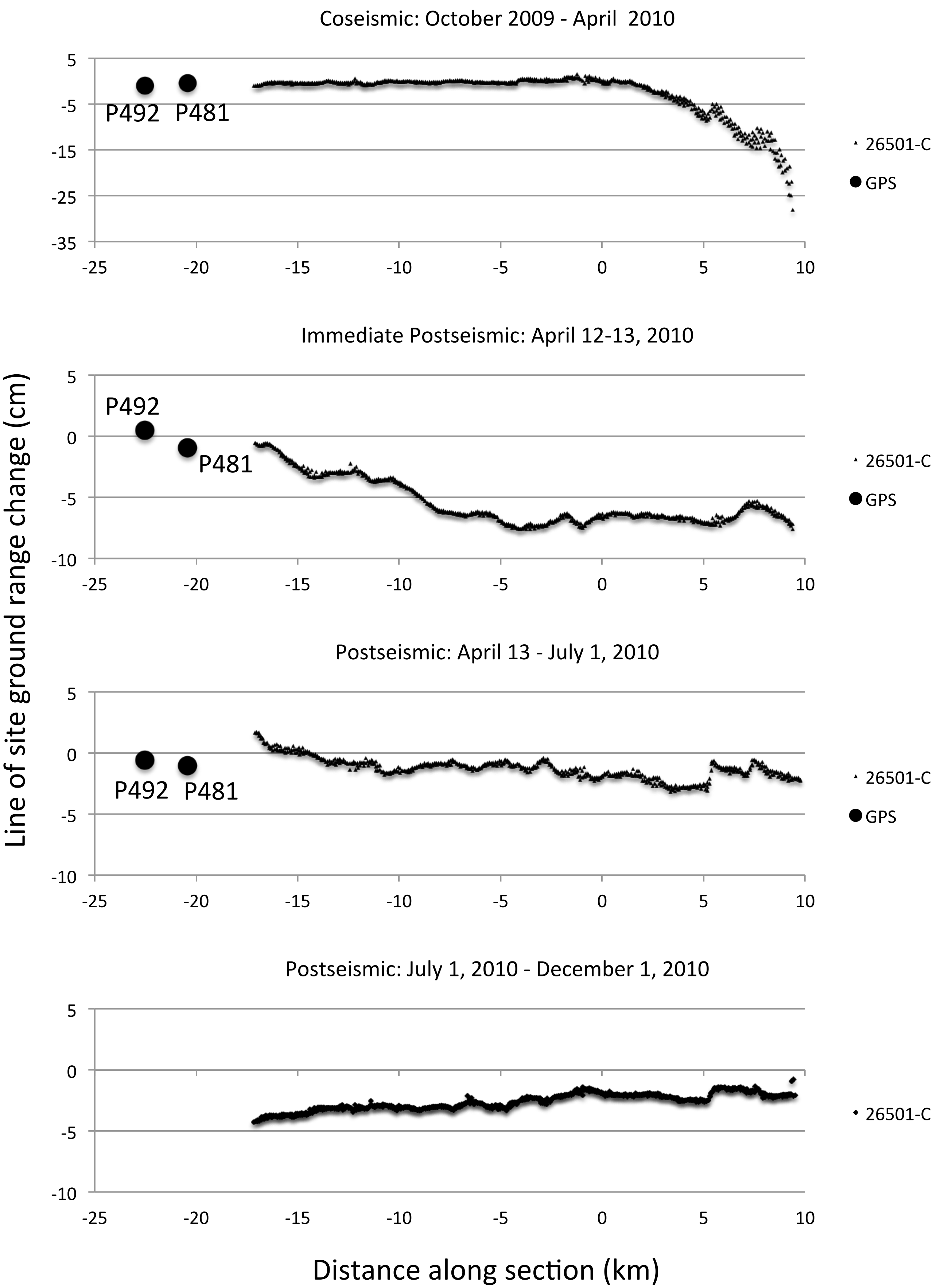
Coseismic: October 2009 - April 2010
Immediate Postseismic: April 12-13, 2010
Postseismic: April 13 - July 1, 2010
Postseismic: July 1, 2010 - December 1, 2010
P492
P481
26501-C
GPS
Line of site ground range change (cm)
Distance along section (km)
5
-5
-15
-25
-35
0
-10
-25
-20
-15
-10
-5
0
5
10

Figure 7

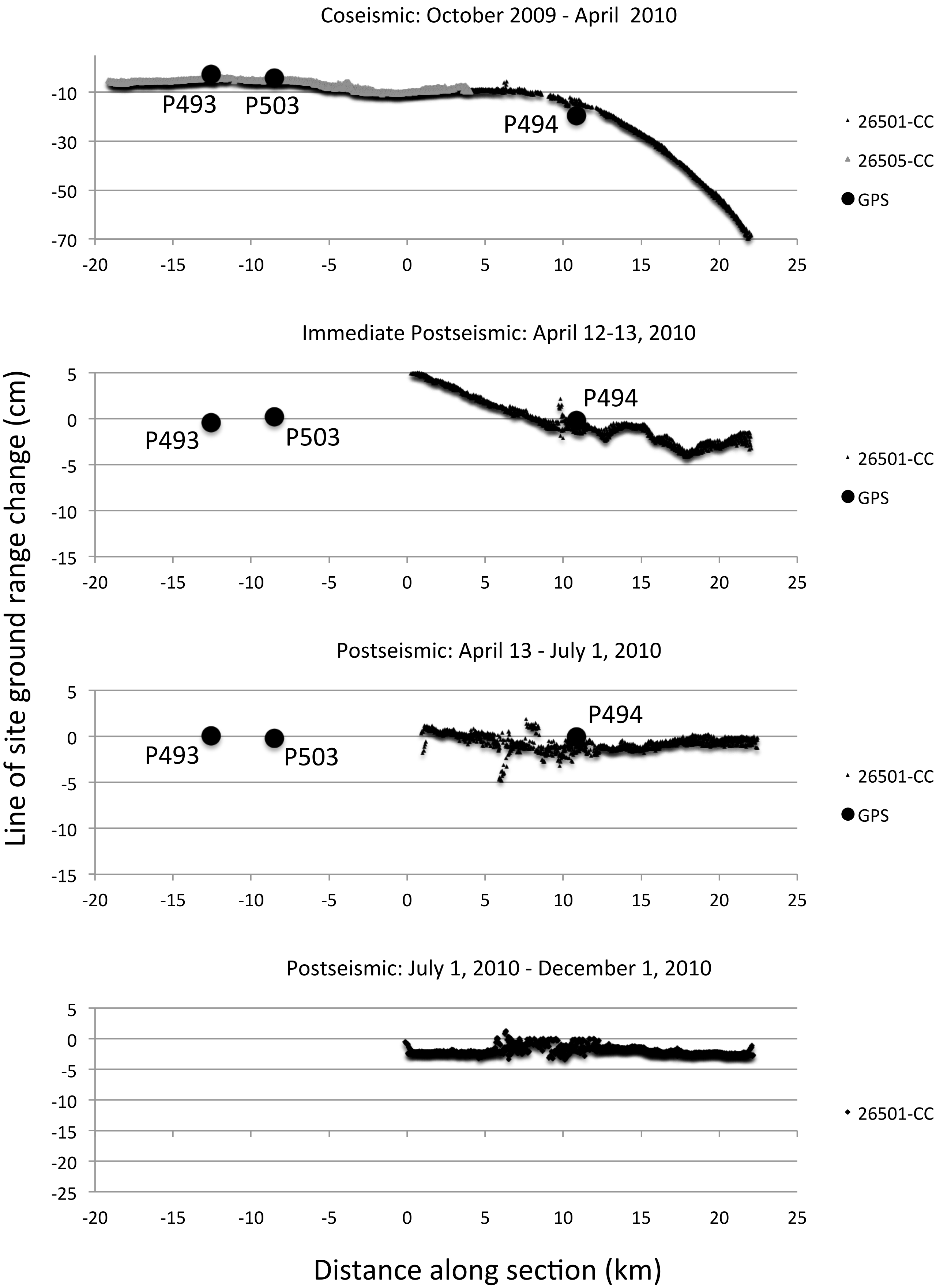

Coseismic: October 2009 - April 2010
P493
P503
P494
26501-CC
26505-CC
GPS
Immediate Postseismic: April 12-13, 2010
P493
P503
P494
26501-CC
GPS
Postseismic: April 13 - July 1, 2010
P493
P503
P494
26501-CC
GPS
Postseismic: July 1, 2010 - December 1, 2010
26501-CC
Line of site ground range change (cm)
Distance along section (km)

Figure 8

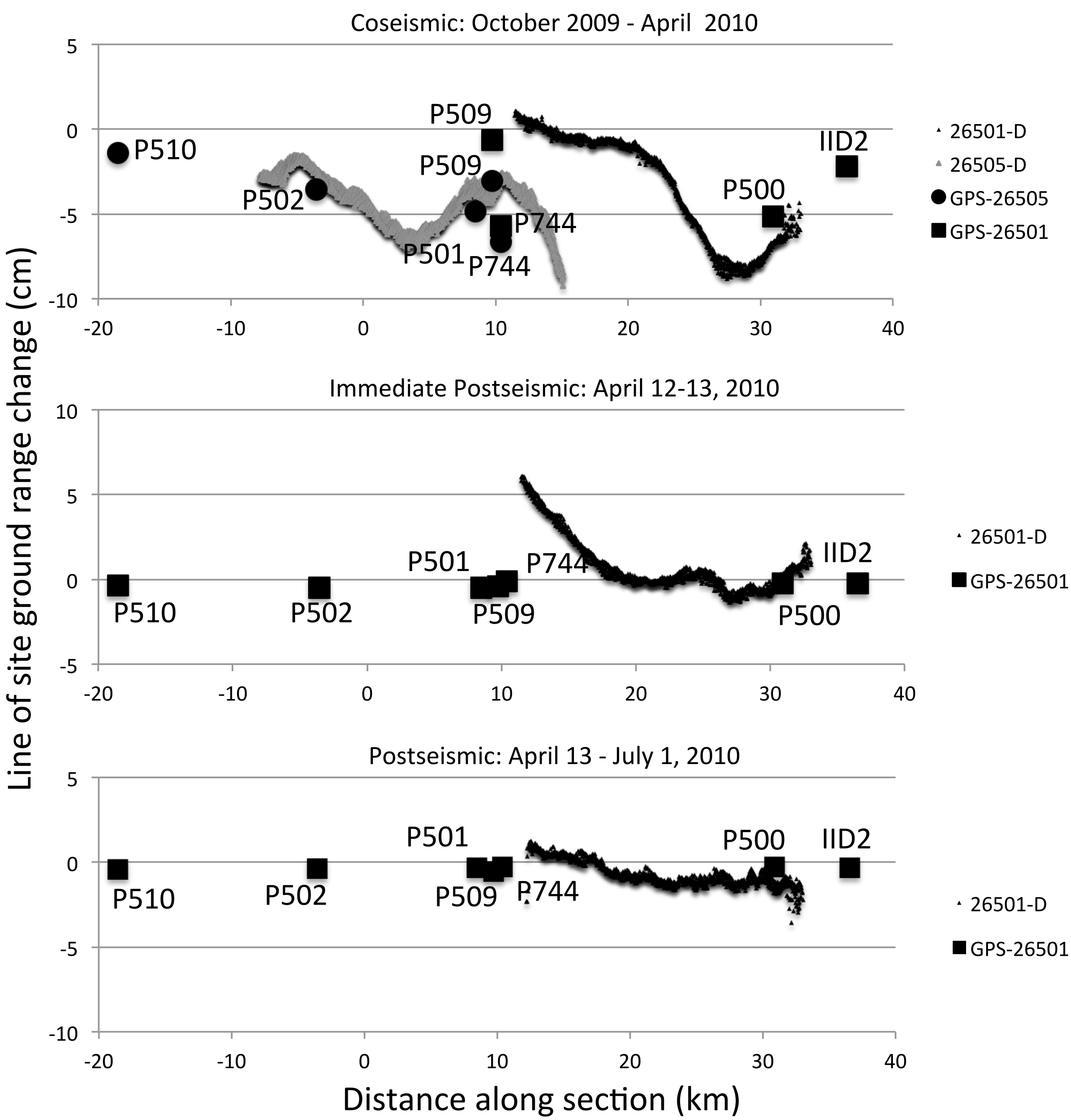

Coseismic: October 2009 - April 2010
P510
P502
P509
P509
P501
P744
P744
P500
IID2
26501-D
26505-D
GPS-26505
GPS-26501
Immediate Postseismic: April 12-13, 2010
P510
P502
P501
P509
P744
P500
IID2
26501-D
GPS-26501
Postseismic: April 13 - July 1, 2010
P510
P502
P501
P509
P744
P500
IID2
26501-D
GPS-26501
Line of site ground range change (cm)
Distance along section (km)

Figure 9

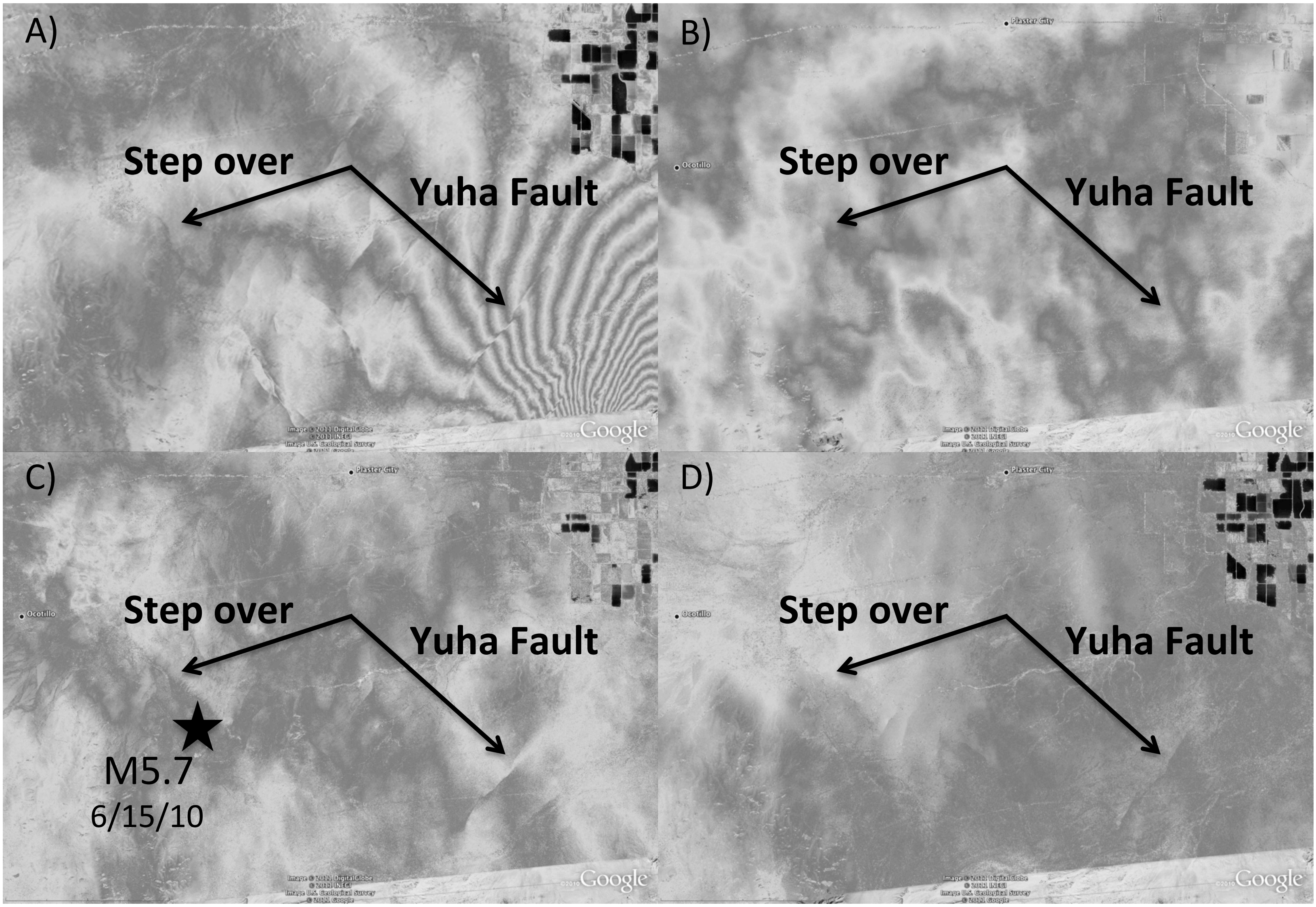

A)
Step over
Yuha Fault
B)
Plaster City
Ocotillo
Step over
Yuha Fault
C)
Plaster City
Ocotillo
Step over
Yuha Fault
M5.7
6/15/10
D)
Plaster City
Ocotillo
Step over
Yuha Fault
Google

Figure 10

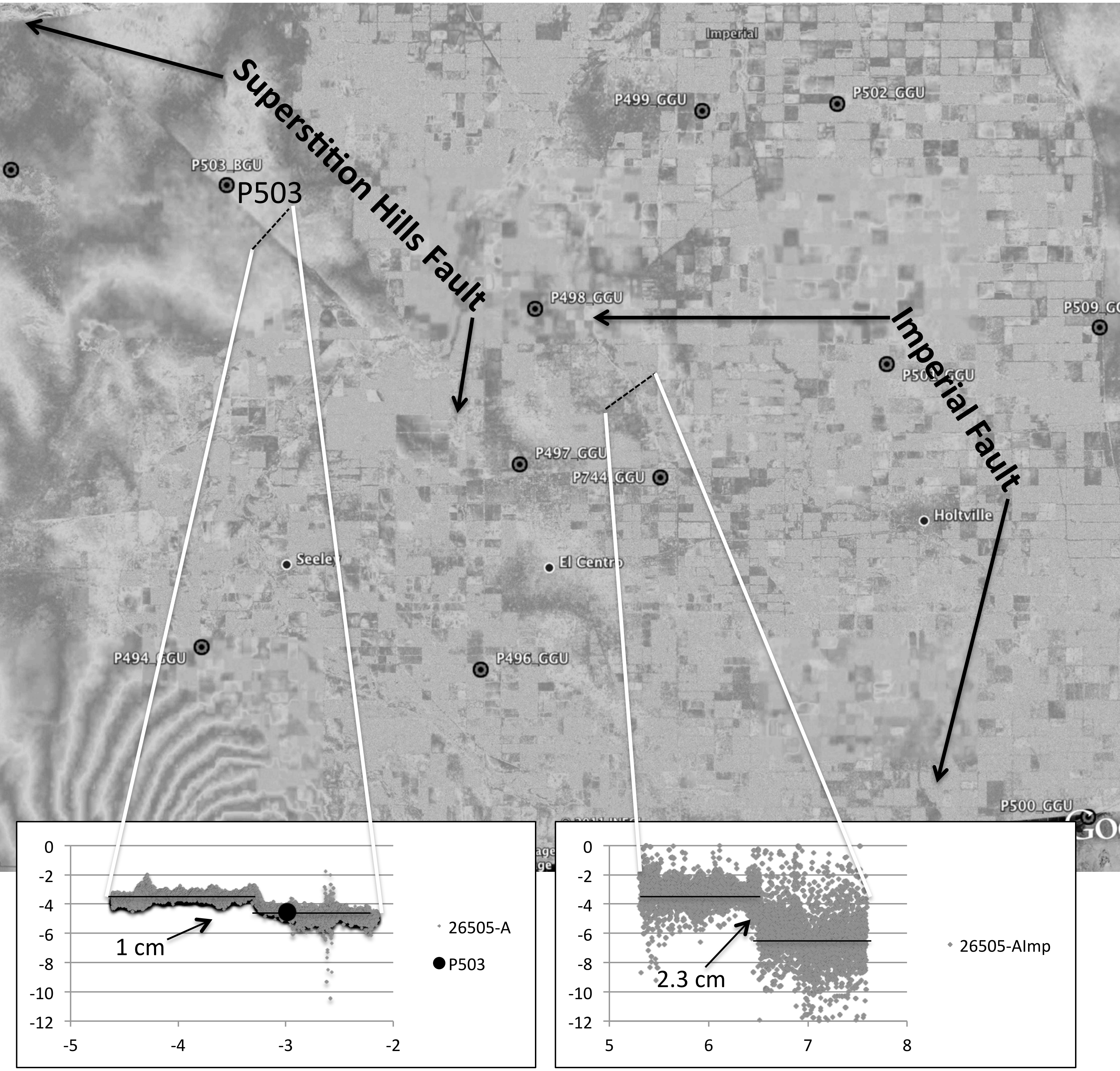

Superstition Hills Fault
Imperial Fault
Imperial
P499_GGU
P502_GGU
P503_BGU
P503
P498_GGU
P509_GG
P497_GGU
P744_GGU
Holtville
Seeley
El Centro
P494_GGU
P496_GGU
P500_GGU
0
-2
-4
-6
-8
-10
-12
-5
-4
-3
-2
1 cm
26505-A
P503
0
-2
-4
-6
-8
-10
-12
5
6
7
8
2.3 cm
26505-AImp

Figure 11

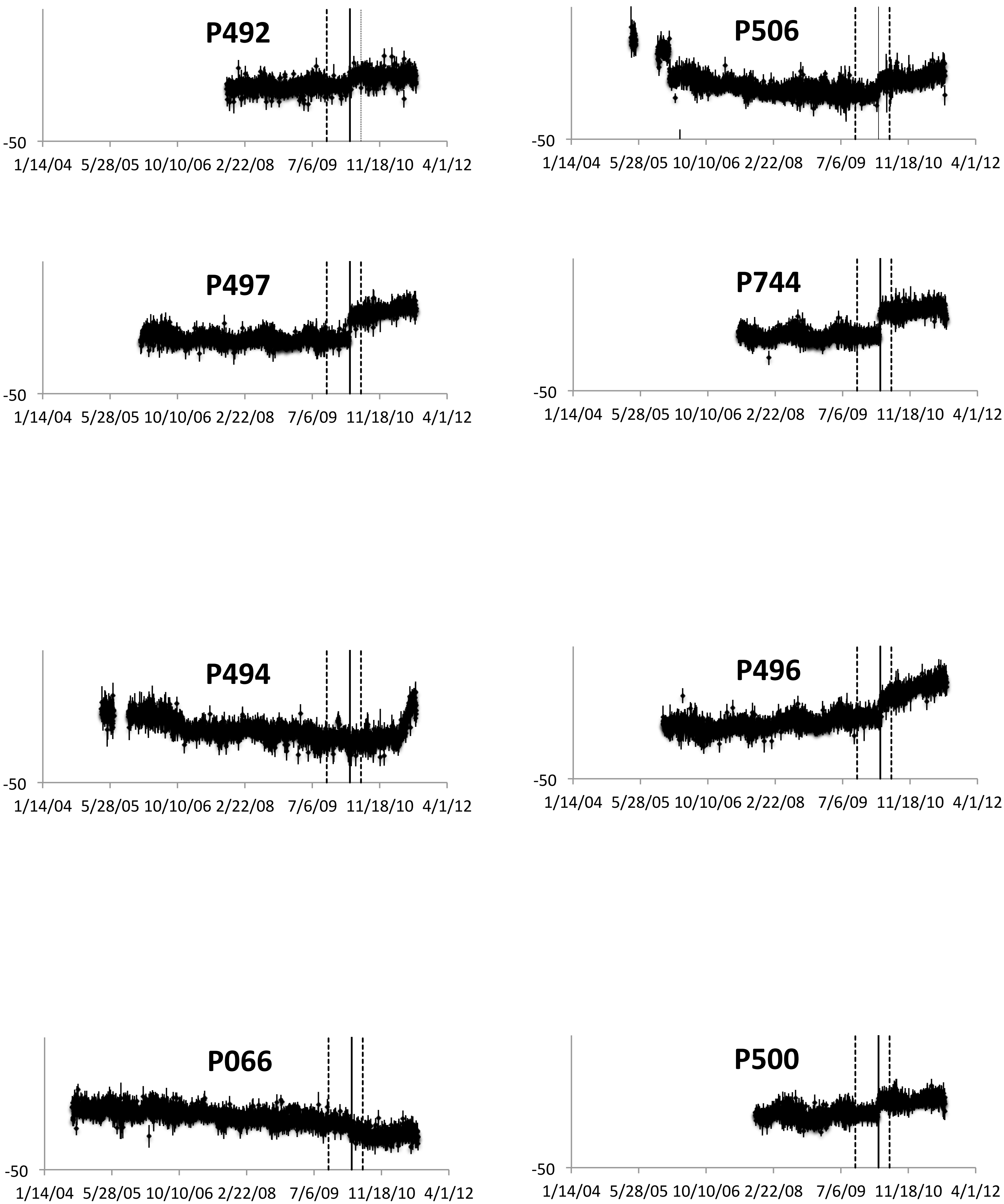
P492
P506
P497
P744
P494
P496
P066
P500
-50
1/14/04 5/28/05 10/10/06 2/22/08 7/6/09 11/18/10 4/1/12

Figure 12

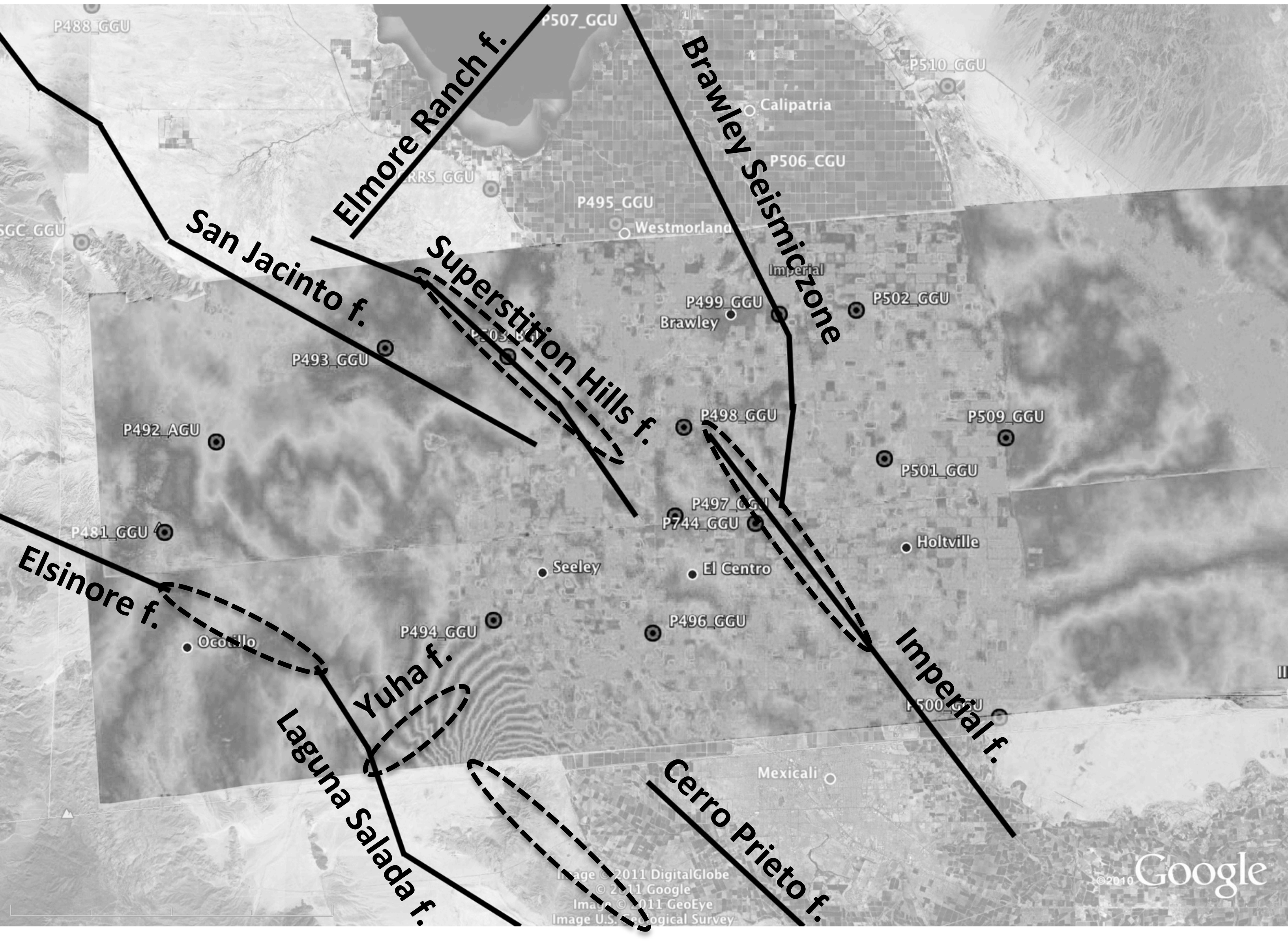

Elmore Ranch f.
Brawley Seismic zone
San Jacinto f.
Superstition Hills f.
Elsinore f.
Yuha f.
Laguna Salada f.
Imperial f.
Cerro Prieto f.
P488_GGU
P507_GGU
P510_GGU
Calipatria
P506_CGU
P495_GGU
Westmorland
Imperial
P499_GGU
Brawley
P502_GGU
P493_GGU
P492_AGU
P498_GGU
P509_GGU
P501_GGU
P497_GGU
P744_GGU
P481_GGU
Holtville
Seeley
El Centro
P494_GGU
P496_GGU
Ocotillo
Mexicali
Google

Copyright Material

Supporting Nonprint Material